RSC Advances

PAPER

View Article Online
View Journal | View Issue

Cite this: *RSC Adv.*, 2017, **7**, 18508

3D dendritic-Fe_2O_3@C nanoparticles as an anode material for lithium ion batteries

Xiaohua Zhang,[a] Zhongfu Zhou, *[bcd] Jinyan Ning,[e] Salma Nigar,[a] Tingkai Zhao,[f] Xionggang Lu[b] and Huaqiang Cao[g]

Received 30th January 2017
Accepted 15th March 2017

DOI: 10.1039/c7ra01260h

rsc.li/rsc-advances

3D dendritic Fe_2O_3 nanoparticles wrapped with carbon (denoted as 3DD-Fe_2O_3@C hereafter) were synthesized. It is found that the 3DD-Fe_2O_3@C is composed of α-Fe_2O_3 and amorphous carbon. As an anode material for lithium ion batteries (LIBs), it exhibits an excellent discharge/charge capacity (982 mA h g^{-1} and 971 mA h g^{-1} after 100 cycles at a rate of 100 mA g^{-1}), and good cyclic stability and rate capability.

As energy storage devices, lithium-ion batteries (LIBs) have been widely used in portable electronic devices, mobile power stations, electrical automotive vehicles *etc.* Graphite as the most commonly used anode material in commercial LIBs, has a stable anode performance, but it is limited due to its low theoretical capacity (372 mA h g^{-1}).[1] Thus, developing alternative electrodes with high capacity has been one of the most urgent tasks in advancing the overall performance of LIBs.[2,3] Among the available candidates, nanometre-sized transition metal oxides have been attracting research attention due to their low cost, wide availability, and especially higher theoretical specific capacities (>600 mA h g^{-1}).[4,5] Iron oxide, as an important member of these transition metal oxides, is regarded as a potential electrode material to replace graphite owing to its much higher theoretical capacity (~1005 mA h g^{-1}) than most other oxides, natural abundance and non-toxicity.[6,7] However the poor electrical conductivity and large volume change during the lithiation/delithiation processes and subsequent pulverization of particles result in rapid cycling performance dropping, which severely encumbers its practical application.[8] The widely used methods to overcome these drawbacks is to form a layer of conducting materials, such as carbon,[9–12] graphene[13–15] and conducting polymers,[16] to wrap the oxide particles. These wrapping layers, can act as buffers which preventing the agglomeration of the nanomaterials and cushioning the volume changes during the lithiation/delithiation processes. Among these wrapping candidates, amorphous carbon is the most commonly used and it can be prepared easily. Amorphous carbon wrapped Fe_2O_3 nanocomposites have been regarded as potential anode materials for LIBs and studied.[17,18] We demonstrate here, a special 3DD-Fe_2O_3@C nanostructured anode material can be synthesized *via* a simple route, it exhibits high capacity and cyclic performance. To date, there has been no work reported about the material with same structure as electrode for LIBs.

Experimental

Fe_2O_3 powder was prepared by a simple hydrothermal method: 0.11 g potassium ferrocyanide ($K_3[Fe(CN)_6]$), 3.8 g polyvinyl pyrrolidone (PVP) and 0.06 g hexadecyl trimethyl ammonium bromide (CTAB) were dissolved into 40 mL deionized water and then the solution was stirred for 30 min, and then was transferred to a 50 mL Teflon-lined stainless autoclave and maintained at 180 °C for 24 h in a rotary oven. The resulted red solid was collected by centrifugation, and then washed with deionized water and ethanol each for several times to remove the soluble impurities after the autoclave was cooled to room temperature naturally. Finally, the product was obtained by dehydrating at 50 °C in an oven overnight.

To synthesize 3DD-Fe_2O_3@C, 0.05 g as-prepared Fe_2O_3 and 0.2 g glucose were dispersed into 16 mL deionized water. After ultrasonic treatment for 15 min, the solution was transferred into a Teflon-lined stainless autoclave for hydrothermal reaction at 180 °C for 4 h in rotary oven. After the autoclave cooled down, the sample was washed with deionized water and absolute ethanol, then was dried in air at 80 °C for 5 h. The 3DD-Fe_2O_3@C was obtained by calcining the above precipitate at 400 °C for 2 h in Ar atmosphere.

X-ray diffraction (XRD) patterns were collected on a 18 kW D/MAX2500V+/PC with Cu Kα radiation at a scan speed of 4° min^{-1}. Scanning electron microscopy (FESEM) images were

[a]*School of Material Science and Engineering, Shanghai University, Shanghai 200444, PR China*
[b]*State Key Laboratory of Advanced Special Steel, Shanghai University, Shanghai 200072, PR China. E-mail: z.zhou@shu.edu.cn*
[c]*Key Laboratory of Material Microstructures, Shanghai University, Shanghai 200444, PR China*
[d]*Department of Physics, Aberystwyth University, Aberystwyth SY23 3BZ, UK*
[e]*Materials Genome Institute, Shanghai University, Shanghai 200444, PR China*
[f]*State Key Laboratory of Solidification Processing, School of Materials Science and Engineering, Northwestern Polytechnical University, Xi'an 710072, PR China*
[g]*Department of Chemistry, Tsinghua University, Beijing 100084, PR China*

acquired on a JEOL JSM-6700F. Transmission electron microscopy images were taken on a JEOL JEM-2010F and a JEOL JEM-2100F. Thermogravimetric analysis (TGA) curve was measured on an MAX700 thermal analyzer.

Electrochemical properties were investigated using CR2032-type coin cells. The working electrode consists of 60% of the active material, 30% of conducting carbon black (Super-P-L), and 10% of polymer binder (polyvinylidene fluoride, PVDF). The electrolyte is 1.0 M $LiPF_6$ in a mixture of ethylene carbonate, ethylmethyl carbonate and diethyl carbonate (EC/EMC/DMC, 1 : 1 : 1 vol). Celgard 2400 was used as the separator and lithium as the counter electrode. Coin-type cells were assembled in an argon-filled glove box (Super 1220/750). Charge–discharge tests were carried out at the voltage range of 0.05–3.0 V (*vs.* Li/Li^+) using a battery test system (BTSDA).

Structure and morphology

The as prepared sample is characterized by XRD. As shown in Fig. 1(a), the obtain Fe_2O_3 is the well crystallized rhombohedral phase of α-Fe_2O_3 (JCPDS no. 33-0664). Furthermore, it implies that the carbon coating treatment on the surface does not change the crystal structure of the sample. There is no distinguishable diffraction peaks associated with carbonaceous crystals found in the pattern, which indicates that the carbon shell is very likely in amorphous state.

The XPS survey spectra of the Fe_2O_3 and 3DD-Fe_2O_3@C are shown in Fig. 1(b). The peaks of Fe, O and C are observed in both the uncoated and coated Fe_2O_3. Furthermore, the relative peak intensity of C 1s of the carbon coated sample is much stronger than that of the uncoated, this indicates the presence of carbon coating. As the atomic sensitivity factor of Fe is considerably higher than those of C and O, the relatively weak intensity of Fe and O in 3DD-Fe_2O_3@C suggest that there is a carbon layer coated on the surface of the 3DD-Fe_2O_3@C.[19] Fig. 1(c) shows the C 1s of the Fe_2O_3 and the 3DD-Fe_2O_3@C samples respectively. We can see that there are only one strong peak centred at 284.6 eV in the 3DD-Fe_2O_3@C associated with C–C bonds. The C 1s spectrum of 3DD-Fe_2O_3 can be resolved into two peaks with binding energies of 284.6 eV and 287.4 eV which can be attributed to the adventitious carbon from the instrument. TGA analysis in Fig. 1(d) shows that the carbon content is about 2.72%.

The morphology of the samples is investigated by SEM. As shown in Fig. 2. The sample show flower-like dendritic nanocrystalline structure with 6 rotational folds. The size of the particles is uniformly of 700–800 nm in diameter. It also can be seen that the size and morphology of dendritic structure are similar before and after the process of carbon coating. The elemental mapping results (Fig. 2(f)–(h)) demonstrate that the distribution patterns of iron and oxygen are coincide, and carbon is well distributed in the sample. This suggests that carbon has been coated onto the entire surface of Fe_2O_3 nanoparticles.

Electrochemical characterization

Electrochemical performance of the Fe_2O_3 and 3DD-Fe_2O_3@C samples has been investigated and is summarized in Fig. 3. Fig. 3(a) shows their charges capacities under current density of 100 mA g^{-1}. It can be seen that the discharge and charge capacities of Fe_2O_3 are 2052 mA h g^{-1} and 1276 mA h g^{-1} respectively in the first cycle, but drop significantly to 320 mA h g^{-1} and 322 mA h g^{-1} after 100 cycles. In comparison, the

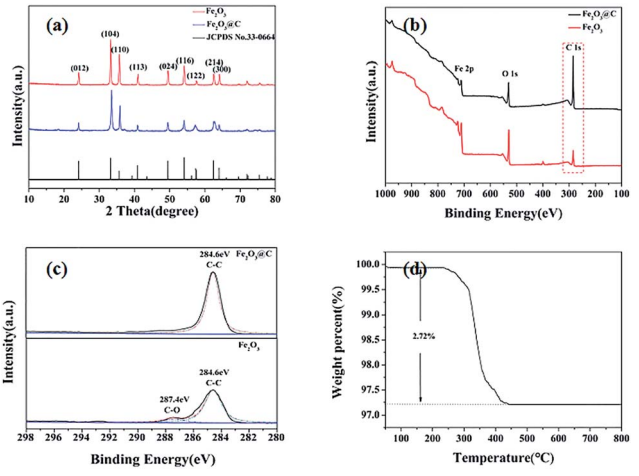

Fig. 1 XRD patterns of Fe_2O_3 and 3DD-Fe_2O_3@C (a); XPS survey spectra (b) and high-resolution XPS spectra of C 1s (c); TGA curves of 3DD-Fe_2O_3@C sample from 25 to 800 °C with heating rate of 10 °C min^{-1} in flowing air (d).

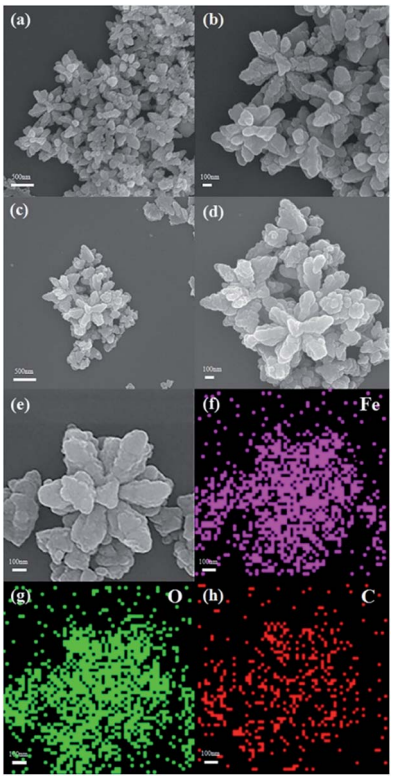

Fig. 2 SEM images of Fe_2O_3 (a and b); SEM images (c–e) and the EDS elemental mapping (f–h) of 3DD-Fe_2O_3@C.

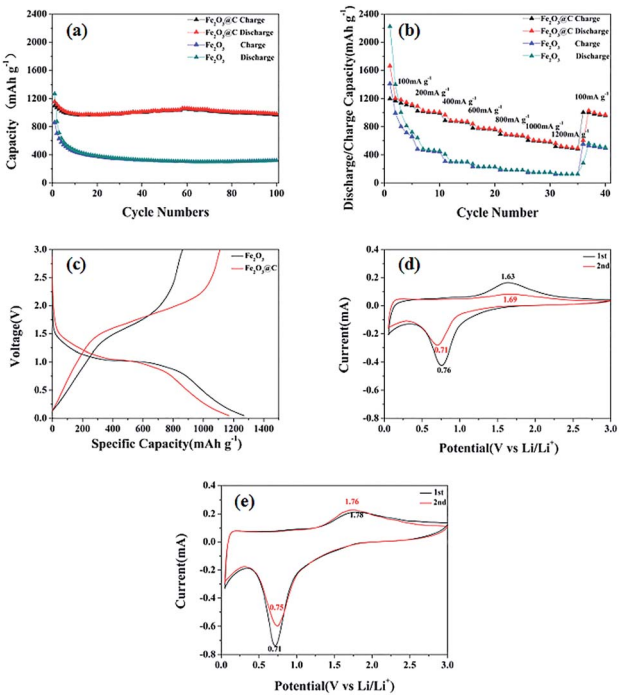

Fig. 3 Cycle performances (a), rate capability (b), first-cycle discharge/charge voltage profiles (c) and CV curves of Fe_2O_3 (d) and 3DD-Fe_2O_3@C (e).

discharge and charge capacities of 3DD-Fe_2O_3@C of the first cycle are 1528 mA h g^{-1} and 1053 mA h g^{-1}, which are much lower than that of uncoated Fe_2O_3. However, after 100th cycle, the discharge and charge capacity of 3DD-Fe_2O_3@C can still remains at 982 mA h g^{-1} and 971 mA h g^{-1}. The rate capacities of the samples are tested from 100 to 1200 mA g^{-1} (100, 200, 400, 600, 800, 1000 and 1200 mA g^{-1}), the current densities for the 5th cycles are displayed in Fig. 3(b). 3DD-Fe_2O_3@C exhibits overall better rate performance against pure Fe_2O_3. The initial discharge capacity of 3DD-Fe_2O_3@C at 100 mA g^{-1} is 1119 mA h g^{-1}. After the testing cycles, the specific capacity of 3DD-Fe_2O_3@C recovers to 972 mA h g^{-1} when the current density is returned to 100 mA g^{-1}. Fig. 3(c) gives the first-cycle discharge/charge voltage profiles in the voltage window of 0.05–3.0 V. The first-cycle discharge/charge capacities of and the uncoated and coated Fe_2O_3 are 1270/862 mA h g^{-1} and 1169/1109 mA h g^{-1}, which result in the coulombic efficiencies of 68% and 95%, respectively. The CV curves of the samples after the first cycle at 100 mA g^{-1} are presented in Fig. 3(d) and (e). The voltage window is 0.05–3 V and scan rate is set to 0.1 mV s^{-1}. In Fig. 3(d), there is a cathodic peak centred at 0.76 V in the 1st scanning cycle, corresponding to the reduction of Fe_2O_3 with lithium ion to form Fe and Li_2O, and the formation of solid electrolyte interphase layer on the surface of the electron. The main anodic peak at 1.63 V is attributed to the oxidation reaction of Fe to form Fe^{3+}.[19,20] In the 2nd cycle, the cathodic and anodic peaks are shifted due to the polarization in the first cycle. The redox peaks of the 3DD-Fe_2O_3@C in Fig. 3(e) at 0.71/1.78 V are close to those of the pure Fe_2O_3, but they show better repeatability.

Conclusions

A 3DD-Fe_2O_3@C LIB anode material has been successfully fabricated through a facile and easy scale-up two-step route. Compared with bare dendritic Fe_2O_3, the 3DD-Fe_2O_3@C exhibit an excellent overall performance. Its discharge/charge capacity can be well remained at 982 mA h g^{-1} and 971 mA h g^{-1} after 100 cycles at a rate of 100 mA g^{-1}. The carbon coating increases significantly the cycling stability of Fe_2O_3. In view of the special structure and outstanding electrochemical performance, the 3DD-Fe_2O_3@C might serve as a potential electrode material for LIBs.

Acknowledgements

This research was supported by NSFC (No. 51371112), Innovation Program of Shanghai Municipal Education Commission (No. 2014CB643403), and National Science Fund for Distinguished Young Scholars of China (No. 51225401). Z. Z. acknowledge the provision of characterization facility by Key Laboratory of Materials Microstructures, Shanghai University, under the visiting professorship scheme.

Notes and references

1 H. Buqa, D. Goers, M. Holzapfel, M. E. Spahr and P. Novak, *J. Electrochem. Soc.*, 2005, **152**, A474–A481.
2 M. Armand and J. M. Tarascon, *Nature*, 2008, **451**, 652–657.
3 J. M. Tarascon and M. Armand, *Nature*, 2001, **414**, 359–367.
4 Z. Li, B. Li, L. Yin and Y. Qi, *ACS Appl. Mater. Interfaces*, 2014, **6**, 8098–8107.
5 P. Poizot, S. Laruelle, S. Grugeon, L. Dupont and J. M. Tarascon, *Nature*, 2000, **407**, 496–499.
6 H. Liu, G. Wang, J. Park, J. Wang, H. Liu and C. Zhang, *Electrochim. Acta*, 2009, **54**, 1733–1736.
7 W. Xiao, Z. Wang, H. Guo, Y. Zhang, Q. Zhang and L. Gan, *J. Alloys Compd.*, 2013, **560**, 208–214.
8 C. K. Chan, H. Peng, G. Liu, K. McIlwrath, X. F. Zhang, R. A. Huggins and Y. Cui, *Nat. Nanotechnol.*, 2008, **3**, 31–35.
9 Z. Li, N. Liu, X. Wang, C. Wang, Y. Qi and L. Yin, *J. Mater. Chem.*, 2012, **22**, 16640.
10 C. Wang, L. Yin, D. Xiang and Y. Qi, *ACS Appl. Mater. Interfaces*, 2012, **4**, 1636–1642.
11 W.-M. Zhang, X.-L. Wu, J.-S. Hu, Y.-G. Guo and L.-J. Wan, *Adv. Funct. Mater.*, 2008, **18**, 3941–3946.
12 J. Liu, D. Qian, H. Feng, J. Li, J. Jiang, S. Peng and Y. Liu, *J. Mater. Chem. A*, 2014, **2**, 11372.
13 H. Wang, L. F. Cui, Y. Yang, H. Sanchez Casalongue, J. T. Robinson, Y. Liang, Y. Cui and H. Dai, *J. Am. Chem. Soc.*, 2010, **132**, 13978–13980.
14 S. Yang, X. Feng, S. Ivanovici and K. Mullen, *Angew. Chem.*, 2010, **49**, 8408–8411.
15 J. Liu, J. Jiang, D. Qian, G. Tan, S. Peng, H. Yuan, D. Luo, Q. Wang and Y. Liu, *RSC Adv.*, 2013, **3**, 15457.
16 F. Wu, J. Chen, R. Chen, S. Wu, L. Li, S. Chen and T. Zhao, *J. Phys. Chem. C*, 2011, **115**, 6057–6063.

17 C. Wu, X. Li, W. Li, B. Li, Y. Wang, Y. Wang, M. Xu and L. Xing, *J. Power Sources*, 2014, **251**, 85–91.
18 F. Qin, K. Zhang, L. Zhang, J. Li, H. Lu, Y. Lai, Z. Zhang, Y. Zhou, Y. Li and J. Fang, *Dalton Trans.*, 2015, **44**, 2150–2156.
19 J. Wang, M. Gao, H. Pan, Y. Liu, Z. Zhang, J. Li, Q. Su, G. Du, M. Zhu, L. Ouyang, C. Shang and Z. Guo, *J. Mater. Chem. A*, 2015, **3**, 14178–14187.
20 N. Liu, J. Shen and D. Liu, *Electrochim. Acta*, 2013, **97**, 271–277.